Joule

Article

Molecular coordination stabilizes built-in electric fields for efficient perovskite solar cells

Graphical abstract

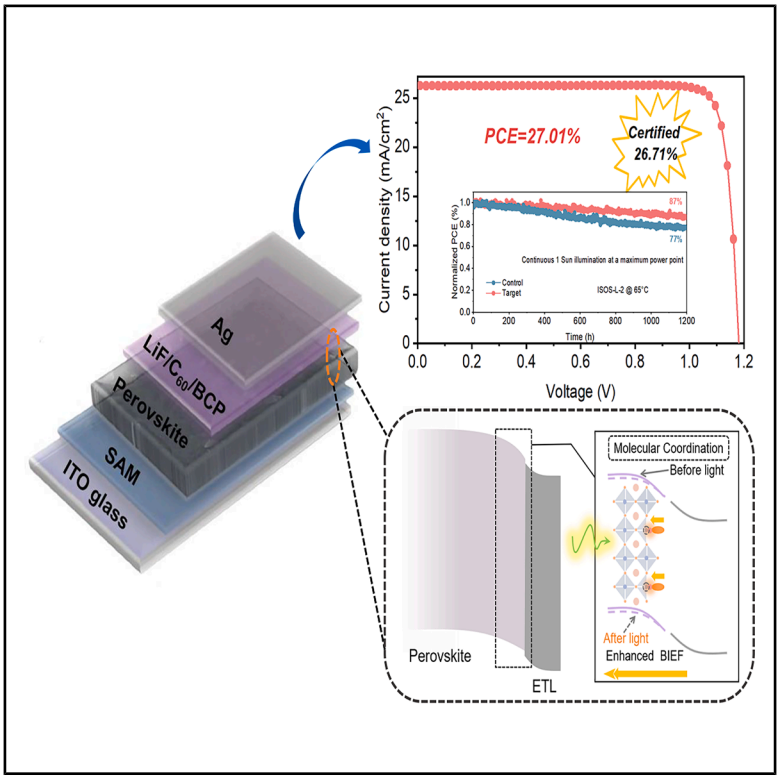

Highlights

- Molecular coordination strategy enables stable BIEFs
- It achieves effective defect passivation and favorable interfacial contact in the device
- The inverted device produces a high efficiency of 27.01% (certified 26.71%)

Authors

Ying Chen, Dejian Yu, Xiaosong Qiu, ..., Ying Li, Tae-Woo Lee, Guichuan Xing

Correspondence

guoj276@mail.sysu.edu.cn (J.G.), queenly@szu.edu.cn (Y.L.), gcxing@um.edu.mo (G.X.)

In brief

A molecular coordination strategy via surface treating perovskite with 2,4,6-tris[3-(diphenylphosphinyl)phenyl]-1,3,5-triazine (PO-T2T) is proposed to construct robust BIEFs and reduce interface defects. The champion perovskite solar cell achieves an efficiency of up to 27.01% (certified 26.71%) with improved long-term stability.

Chen et al., 2026, Joule *10*, 102484
October 21, 2026
https://doi.org/10.1016/j.joule.2026.102484

CellPress

Joule

CellPress

Article

Molecular coordination stabilizes built-in electric fields for efficient perovskite solar cells

Ying Chen,[1,2,9] Dejian Yu,[1,9] Xiaosong Qiu,[1,9] Hao Gu,[1] Jia Guo,[3,*] Yuexin Lin,[4] Bingzhe Wang,[5] Junmin Xia,[6,7] Tao Sheng,[1] Shengwen Li,[1] Shi Chen,[1] Chao Liang,[4] Ying Li,[2,*] Tae-Woo Lee,[8] and Guichuan Xing[1,10,*]

[1]Joint Key Laboratory of the Ministry of Education, Institute of Applied Physics and Materials Engineering, University of Macau, Avenida da Universidade, Taipa, Macau 999078, P.R. China

[2]International Collaborative Laboratory of 2D Materials for Optoelectronic Science & Technology of Ministry of Education, Institute of Microscale Optoelectronics, Shenzhen University, Shenzhen 518060, China

[3]School of Flexible Electronics (SoFE), Sun Yat-sen University, 66 Gongchang Road, Shenzhen, Guangdong 518107, China

[4]State Key Laboratory of Electrical Insulation and Power Equipment, School of Physics, Xi'an Jiaotong University, Xi'an 710049, P.R. China

[5]College of Chemistry and Materials Science, Guangdong Provincial Key Laboratory of Supramolecular Coordination Chemistry, Jinan University, Guangzhou 510632, China

[6]State Key Laboratory of Flexible Electronics (LoFE), Institute of Advanced Materials (IAM), Nanjing University of Posts & Telecommunications, 9 Wenyuan Road, Nanjing 210023, China

[7]Guangdong Provincial Key Laboratory of Semiconductor Optoelectronic Materials and Intelligent Photonic Systems, Harbin Institute of Technology, Shenzhen 518055, China

[8]Department of Materials Science and Engineering, Institute of Engineering Research, Research Institute of Advanced Materials, Soft Foundry, Interdisciplinary Program in Bioengineering, Seoul National University, Seoul, Republic of Korea

[9]These authors contributed equally

[10]Lead contact

*Correspondence: guoj276@mail.sysu.edu.cn (J.G.), queenly@szu.edu.cn (Y.L.), gcxing@um.edu.mo (G.X.)

https://doi.org/10.1016/j.joule.2026.102484

CONTEXT & SCALE The built-in electric field (BIEF), vital for the operation of perovskite solar cells (PSCs), is established by minority carrier accumulation near the interface. However, under illumination, the density of the photoinjected electron-hole pairs far exceeds the intrinsic carrier density in perovskites. Therefore, the space charge is dynamically screened because of electrostatic shielding, thereby weakening the built-in potential. This screening effect fundamentally contradicts the requirement for stable BIEFs in high-efficiency PSCs. Herein, our approach concentrates 2,4,6-tris[3-(diphenylphosphinyl)phenyl]-1,3,5-triazine (PO-T2T) molecules in the depletion region near the perovskite/electron transport layer (ETL) interface. PO-T2T molecules coordinate with undercoordinated Pb^{2+} in the perovskite, forming high-density local molecular dipoles ($\sim 10^{16}$ cm^{-3}) that strengthen the BIEF against the illumination screening. Concomitantly, the coordination strategy enables effective defect passivation and favorable interfacial energy band alignment for carrier extraction, thereby enabling high-performance devices. This work provides crucial theoretical guidance for designing the next-generation photostable photovoltaics.

SUMMARY

The efficiency of perovskite solar cells (PSCs) based on bulk heterojunctions fundamentally relies on their built-in electric fields (BIEFs) to drive charge carrier separation and extraction. However, high-quality perovskite films usually exhibit an intrinsically low carrier density ($\sim 10^{14}$ cm^{-3}) compared with the photoinjected electron-hole pair density (10^{15}–10^{16} cm^{-3}) under 1-sun illumination. This fundamental contradiction makes BIEFs vulnerable to dynamical screening under operational conditions. Herein, we report a molecular coordination strategy to stabilize the BIEF with 2,4,6-tris[3-(diphenylphosphinyl)phenyl]-1,3,5-triazine (PO-T2T). By creating a concentration gradient near the perovskite surface, PO-T2T effectively coordinates with undercoordinated Pb^{2+} sites to form high-density local dipoles ($\sim 10^{16}$ cm^{-3}), significantly

Please cite this article in press as: Chen et al., Molecular coordination stabilizes built-in electric fields for efficient perovskite solar cells, Joule (2026), https://doi.org/10.1016/j.joule.2026.102484

stabilizing the BIEF under illumination. Consequently, the resulting PSC delivers a power conversion efficiency (PCE) of 27.01% (certified 26.71%) with improved operational stability. These results underscore the pivotal role of PO-T2T in suppressing field screening, providing critical insights for designing high-efficiency heterojunction solar cells.

INTRODUCTION

Perovskite solar cells (PSCs) have attracted intense attention in recent years because of their rapidly increasing power conversion efficiency (PCE),[1–4] approaching that of state-of-the-art silicon solar cells. Among them, inverted (p-i-n) PSCs offer remarkable advantages in terms of stability and compatibility in tandem solar cells, positioning them as one of the most promising photovoltaic (PV) technologies.[5–8] To further harness the potential of inverted PSCs, recent studies have identified the interfaces between perovskite and charge transport layers (CTLs) as critical bottlenecks for energy loss. These interfacial losses compromise the quasi-Fermi-level splitting of photogenerated carriers, thereby limiting further advancements in open-circuit voltage (V_{OC}) and PCE.[9,10] While substantial progress has been made in optimizing the perovskite/hole transport layer (HTL) interface through the development of self-assembled monolayers (SAMs),[2,8,11,12] the other interface between the perovskite and the electron transport layer (ETL) has seen limited breakthroughs. In particular, the built-in electric field (BIEF) at the perovskite/ETL heterojunction can be subjected to dynamic screening under illumination, which blunts carrier separation and extraction; however, this critical issue remains rarely explored.

In conventional heterojunction structures, the contact between a relative *p*-type layer and a relative *n*-type layer induces a redistribution of charge carriers, whereby the electrons (as the majority carriers) in the *n*-type region diffuse into the *p*-type side (where electrons act as minority carriers) and vice versa.[10] Such carrier diffusions accumulate minority carriers in the depletion region to establish a BIEF. A high-quality perovskite film with few defects typically exhibits an intrinsically low carrier density of $\sim 10^{14}$ cm^{-3}. However, owing to the exceptional light absorption of perovskite films,[13] the density of photoinjected electron-hole pairs under standard solar illumination can reach 10^{15}–10^{16} cm^{-3}, which far exceeds the intrinsic carrier concentration and is comparable to that in the depletion region (10^{15}–10^{17} cm^{-3}; Note S1).[14–17] This drastic difference means that the BIEF could be easily screened by photoinjected carriers,[18,19] weakening carrier separation and extraction, which leads to non-negligible voltage deficits and compromises device performance.[2,20] Indeed, previous reports have shown that the PCE of PSCs could be dramatically improved upon attenuated illumination,[21,22] aligning with the screening effect of the BIEF. Several attempted strategies might be conducive to strengthening the BIEF, including capping two-dimensional (2D) perovskite layers,[23–25] ferroelectric materials doping,[26] and interface dipole engineering.[20,27] Nevertheless, these approaches primarily rely on passivation to mitigate static BIEF screening by defects, which essentially represents an equilibrium process intended to restore the potential landscape in the dark. Yet, under operational conditions, photoinjection is a nonequilibrium process, generating competing processes between carrier generation and carrier recombination. This induces a dynamic screening effect where accumulated carriers continuously weaken the BIEF. Therefore, achieving a robust and photostable electric field remains a substantial challenge.

Herein, we develop a molecular coordination strategy by using a functionalized molecule, 2,4,6-tris[3-(diphenylphosphinyl)-phenyl]-1,3,5-triazine (PO-T2T), to establish a stable BIEF near the top perovskite surface in inverted PSCs. The coordination between the electronegative units (P=O) within PO-T2T and undercoordinated Pb^{2+} forms local molecular dipoles to strengthen the BIEF against the illumination screening, as evidenced by depth-profiling ultraviolet photoelectron spectroscopy (DP-UPS), capacitance-voltage (*C-V*) measurements, and *I-V* characteristics of two-terminal devices. Consequently, the modified device shows a significantly smaller efficiency drop under intensified illumination, compared with the control device. Furthermore, the molecular coordination also effectively passivates surface defects. The combined effects of BIEF stabilization and defect passivation yield a high PCE of 27.01% (certified 26.71%) under AM 1.5 G sunlight conditions. The mitigated interfacial instability also enhances the operational stability, enabling the optimized PSC to retain 87% of its initial PCE after continuously operating for 1,200 h at 65°C (ISOS-L-2 protocol) and maintain 89% of its original efficiency in long-term thermal stability tests under 85°C for 1,100 h (ISOS-D-2I protocol). This strategy offers a new perspective for exploring diverse high-efficiency heterojunction solar cells.

RESULTS

Molecular coordination between PO-T2T and perovskite

As undercoordinated Pb^{2+} is one of the primary origins of deep-level defects in perovskite films,[28] effective defect neutralization requires potent Lewis bases capable of robust coordination with Pb^{2+}. In this regard, the P=O group offers significantly stronger Lewis basicity, compared with commonly employed carboxyl or amino groups.[29,30] Furthermore, a specific steric structure is also essential for modulating the interfacial electric field and enabling effective charge extraction. Integrating these chemical and steric design criteria, we selected PO-T2T (chemical structure of the molecule shown in Figure S1), which features a bulky π-conjugated backbone anchored with multiple P=O groups, realizing both defect passivation and interfacial dipole regulation. We started by incorporating PO-T2T molecules directly into the anti-solvent that drives the crystallization of $Cs_{0.05}FA_{0.85}MA_{0.1}PbI_3$ perovskite films. Noticeably, incorporating a small amount of PO-T2T during anti-solvent processing does not form a continuous thin layer on the perovskite surface, which can be verified by the inferior performance of devices with a thermally evaporated

Please cite this article in press as: Chen et al., Molecular coordination stabilizes built-in electric fields for efficient perovskite solar cells, Joule (2026), https://doi.org/10.1016/j.joule.2026.102484

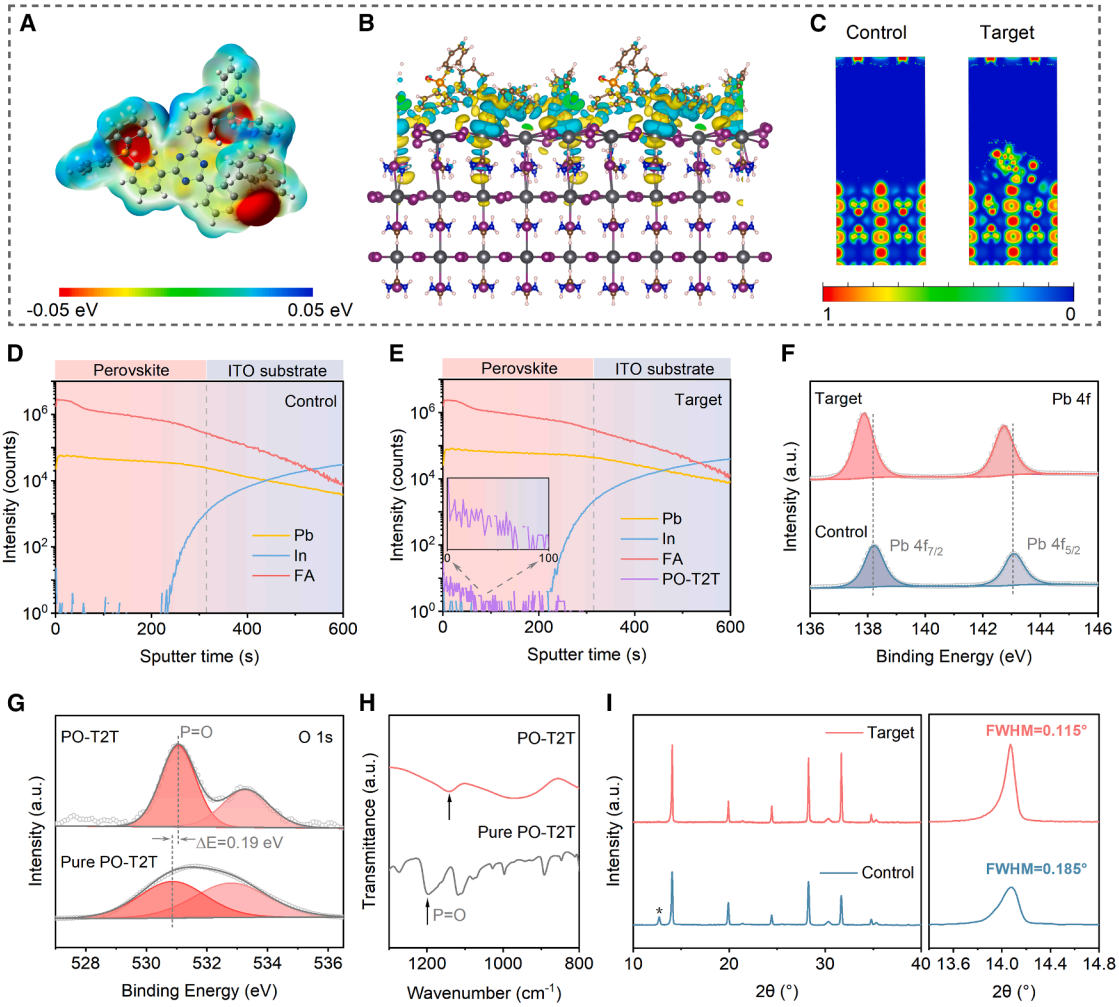

Figure 1. Functionality of PO-T2T interactions with perovskites

(A) Structure and ESP of the PO-T2T molecule.

(B) The CDD of PO-T2T absorbed on the perovskite surface (CDD isosurface = 0.0005). Blue and yellow represent electron depletion and accumulation regions, respectively.

(C) The calculated electron localization function for the region in (B).

(D and E) TOF-SIMS depth-profile results of pristine and PO-T2T-treated perovskite films. The purple line indicates the gradient distribution of PO-T2T within the perovskite layer.

(F) Pb 4f XPS spectra of the control and treated perovskite films.

(G) O 1s XPS spectrum of pure PO-T2T powder, compared with that of perovskite treated with PO-T2T. The shifts of Pb 4f and O 1s characteristic peaks demonstrate the molecular coordination between undercoordinated Pb^{2+} and PO-T2T.

(H) FTIR spectra of pure PO-T2T powder and PO-T2T-treated perovskite films.

(I) XRD spectra of control and treated perovskite films (* denotes PbI_2). Both the increased XRD intensity and reduced FWHM of 3D perovskites illustrate significantly improved crystallinity of the perovskite films.

PO-T2T layer (Figure S2). To investigate the interaction between perovskite and PO-T2T, we performed density functional theory (DFT) calculations. The electrostatic potential (ESP) map of PO-T2T is illustrated in Figure 1A. Theoretically, PO-T2T, with electron-rich units (P=O), is capable of establishing efficient chemical interactions with electron-deficient Lewis acid defects. The charge density difference (CDD) and calculated electron localization function results confirm that the PO-T2T molecules can bind with undercoordinated Pb^{2+} through Lewis acid-base interaction (Figures 1B and 1C). To elucidate the spatial distribution of PO-T2T in the perovskite film, we conducted time-of-flight secondary-ion mass spectrometry (TOF-SIMS) measurement (Figures 1D and 1E). The result reveals a gradual decline in the content of PO-T2T from the top to bottom, establishing a gradual transition in BIEF that benefits charge collection. This distribution is attributed to the rapid top-down crystallization kinetics and the steric hindrance of the bulky PO-T2T molecules,[31] which effectively trap the PO-T2T molecules at the initiation interface, further stabilized by the chemical coordination between the P=O and undercoordinated Pb^{2+}.

Please cite this article in press as: Chen et al., Molecular coordination stabilizes built-in electric fields for efficient perovskite solar cells, Joule (2026), https://doi.org/10.1016/j.joule.2026.102484

Further, X-ray photoelectron spectroscopy (XPS) characterization was carried out to explore the interaction between the molecule and perovskite. We noticed a significant shift of the Pb 4f characteristic peaks to a lower binding energy in treated films, compared with those in the control, indicative of the increased surrounding electron density at Pb^{2+} (Figure 1F). Meanwhile, the shift in the P=O peaks suggests the typical molecular coordination between undercoordinated Pb^{2+} and PO-T2T (Figure 1G).[32] Consistently, Fourier-transform infrared (FTIR) spectra (Figure 1H) reveal the presence of intermolecular interaction between PO-T2T molecules and perovskites, as evidenced by the downshift in the P=O stretching vibrational modes.

We then conducted top-view scanning electron microscopy (SEM) measurements to investigate the morphology of the resultant perovskite films with (target) and without (control) PO-T2T molecules (Figure S3). Compared with the control film (~395 nm), the perovskite film with PO-T2T exhibits an enlarged grain size (~681 nm), in agreement with the result derived from the atomic force microscope (AFM) images (Figure S4). This enlargement can be primarily attributed to the strong interaction between the PO-T2T and undercoordinated Pb^{2+} in the perovskite, which modulates the nucleation and growth kinetics, effectively suppressing the nucleation density and promoting lateral growth of grains. Figure 1I presents the X-ray diffraction (XRD) patterns of the perovskite films. There are no new diffraction peaks or peak shifts in the target film, which indicates that the molecules do not enter the crystal lattice but rather remain at the grain boundaries or surface during film crystallization. This is supported by the identical absorption edges in the ultraviolet-visible (UV-vis) absorption curves (Figure S5). Notably, the PO-T2T-treated film contains negligible residual lead (II) iodide (PbI_2) but shows stronger three-dimensional (3D) perovskite diffraction peaks. Additionally, the target perovskite film exhibits a reduced full width at half maximum (FWHM) of the (110) peak, further suggesting significantly improved film quality. In summary, these results collectively indicate that PO-T2T effectively regulates the crystal growth kinetics, leading to high-quality perovskite films with large grain sizes and enhanced crystallinity.

BIEF stabilization via molecular coordination

Subsequently, we investigated in detail the impact of the molecular coordination between PO-T2T and perovskite on surface energetics. Notably, the conventional UPS measurement is only capable of probing the top few nanometers of surface energetics in perovskite films.[33] Therefore, we carried out DP-UPS to study the energetic landscape at the perovskite interface and within the bulk in the dark (Figures 2B and 2C).[34–36] As depicted in Figure S6, the work functions (WFs) of the unetched control and target perovskite surfaces are measured to be 4.92 and 4.50 eV, respectively. The reduction in WF indicates that the PO-T2T-modified film offers a favorable *n*-type contact at the perovskite/ETL interface. The enhanced *n*-type characteristic of the perovskite film is conducive to suppressing trap-assisted recombination and improving charge extraction.[37,38] The reduced surface contact potential difference (CPD) of the treated film, measured by using Kelvin probe force microscopy (KPFM), further corroborates this result (Figures 2D and S7).[39,40] Importantly, the WF of the control sample remains almost constant with increasing etching time, which means the absence of energetic change throughout the film. In contrast, the target sample exhibits increased WF from surface to bulk, indicating the presence of band bending near the top surface, thus enhancing the driving force for efficient carrier separation. This finding is further confirmed by the higher built-in potential (V_{bi}) of PO-T2T-treated PSC compared with the control device (Figure S8).

Integrating the findings from the above analyses, we posit that the electron-rich units in PO-T2T interact with the perovskite through Lewis acid-base interactions. These interactions facilitate the redistribution of electrons, ultimately establishing the BIEF through molecular coordination. The charge behavior observed in CDD offers evidence for this inference (Figure 1B). Notably, electrons (yellow) accumulate at PO-T2T sites, while holes (blue) gather at the perovskite side, further confirming the existence of BIEF.[41] We then measured the *I-V* characteristics of two-terminal ITO/perovskite/Cu devices under illumination. Theoretically, the close WFs of ITO (~4.7 eV) and Cu (~4.6 eV) should generate a symmetric energy landscape across the device, so that the behavior of the *I-V* curves mainly reflects the energy landscape within the perovskite films.[42] The control device exhibits an ohmic contact property (Figure 2E), which indicates a flat energy landscape throughout the perovskite film. Notably, the *I-V* characteristic does not arise from leakage current, as we are able to detect Schottky junction behavior (Figure S9) if we substitute the Cu electrode with Au (WF ~5.1 eV). In stark contrast, the PO-T2T-treated ITO/perovskite/Cu device presents a rectification characteristic (Figure 2F). This result reveals the presence of a BIEF in the target film, in line with the BIEF enhancement through molecular coordination. More importantly, the rectification characteristic remains even under continuous illumination (Figure S10), which means the intrinsic BIEF is stable against the screening effect. The equivalent dipole generated by the coordination is estimated to be 10^{16}–10^{17} cm^{-3} (Note S2), which is comparable to the photoinjection electron-hole pair density, therefore empowering the perovskite/ETL heterojunction with the anti-screening capability.

Defect passivation in perovskites

The coordination strategy also allows for effective passivation of Pb^{2+} with PO-T2T. To study the passivation effect, we then investigated the influence of PO-T2T molecules on charge carrier dynamics. The target film displays a significant increase in the photoluminescence (PL) intensity, compared with the control film (Figure 3A). Intriguingly, despite the band bending effect, which facilitates carrier separation, the time-resolved photoluminescence (TRPL) characterization (Figure 3B; Table S1) shows a significantly prolonged carrier lifetime after PO-T2T treatment. These results suggest significantly mitigated carrier recombination that even outstrips the charge separation effect with an inverse impact. Besides, when C_{60}, a widely used electron transport material (ETM), covers the top surface, the PO-T2T-incorporated film exhibits relatively weaker PL intensity and reduced carrier lifetime, indicating enhanced charge extraction at the perovskite/ETM interface due to the strengthened BIEF.[43] The Suns-V_{OC} method was then applied to calculate the ideality factor of the devices. The deduced ideality factor decreases from

Please cite this article in press as: Chen et al., Molecular coordination stabilizes built-in electric fields for efficient perovskite solar cells, Joule (2026), https://doi.org/10.1016/j.joule.2026.102484

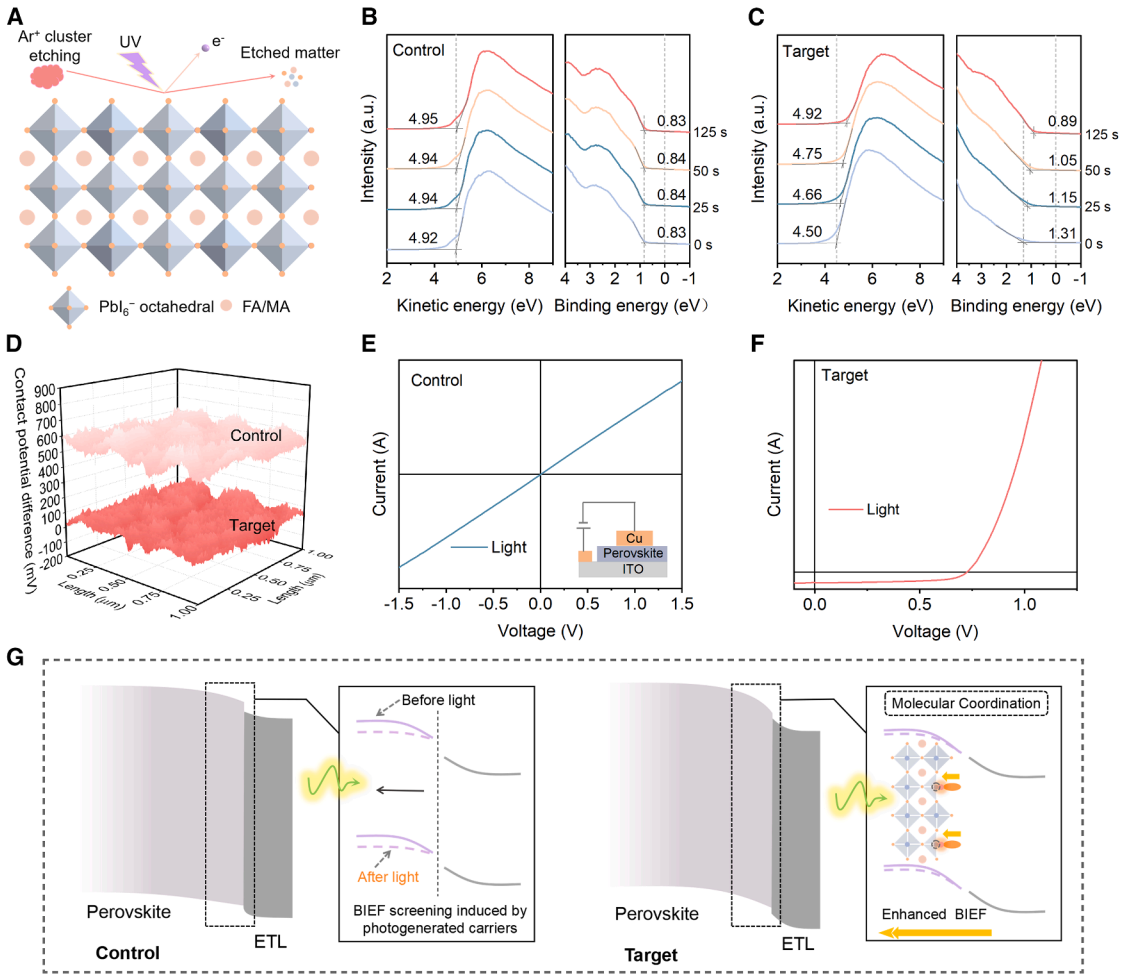

Figure 2. Enhanced and stable BIEF via molecular coordination strategy

(A) Schematic diagram of the UPS depth-profiling technique.

(B and C) Depth-profiling UPS spectra of the control and PO-T2T-treated perovskite films with different etching times. The PO-T2T sample exhibits an increased WF with increasing etching time, indicating the formation of an extra electrical field aligned with BIEF at the interface.

(D) 3D KPFM mappings for the control and treated perovskite films. PO-T2T treatment successfully reduces the surface CPD, which means a decreased WF and the formation of a favorable *n*-type contact at the perovskite/C_{60} interface.

(E and F) The corresponding *I-V* characteristics of the two-terminal control and PO-T2T-treated devices under illumination. The control device exhibits a clear ohmic contact property, while the treated device presents a typical rectification characteristic under illumination, suggesting the formation of photostable internal electric fields after PO-T2T treatment.

(G) Schematic diagram showing the enhanced photostability of the BIEF achieved through molecular coordination.

1.47 (control) to 1.26 (target), which is attributed to the suppression of trap-assisted nonradiative recombination (Figure 3C). This finding is further corroborated by the improved electroluminescence quantum yield (ELQY) and reduced trap-filled limited voltage (V_{TFL}) of PO-T2T devices (Figures S11 and S12). Furthermore, analysis of the calculated local density of states (LDOSs) projected onto surface Pb atoms (Figure 3D) reveals that the defect-induced band-edge tail states are suppressed after introducing PO-T2T, confirming the effectiveness of our passivation strategy.

To gain comprehensive insight into the carrier recombination dynamics within the perovskite film, we conducted femtosecond transient absorption (fs-TA) measurements. Compared with the control film, treatment with PO-T2T exhibits a markedly slow decay, underscoring its efficacy in suppressing defect-assisted recombination (Figure 3E). Furthermore, since the BIEF can suppress surface recombination velocity (SRV) by reducing carrier density at critical interfaces through band bending,[35,44] we derived the SRV from TA data for films of varying thicknesses (Figure S13), with detailed fitting parameters delineated in Table S2. With the PO-T2T treatment, the effective SRV decreases by one order of magnitude, from approximately 1.4×10^3 cm s^{-1} (control) to 6.7×10^2 cm s^{-1} (target) (Figure 3F). The sharp drop in SRV for PO-T2T is consistent with the passivation effect by the molecular coordination strategy. Consequently, the corresponding nonradiative

Please cite this article in press as: Chen et al., Molecular coordination stabilizes built-in electric fields for efficient perovskite solar cells, Joule (2026), https://doi.org/10.1016/j.joule.2026.102484

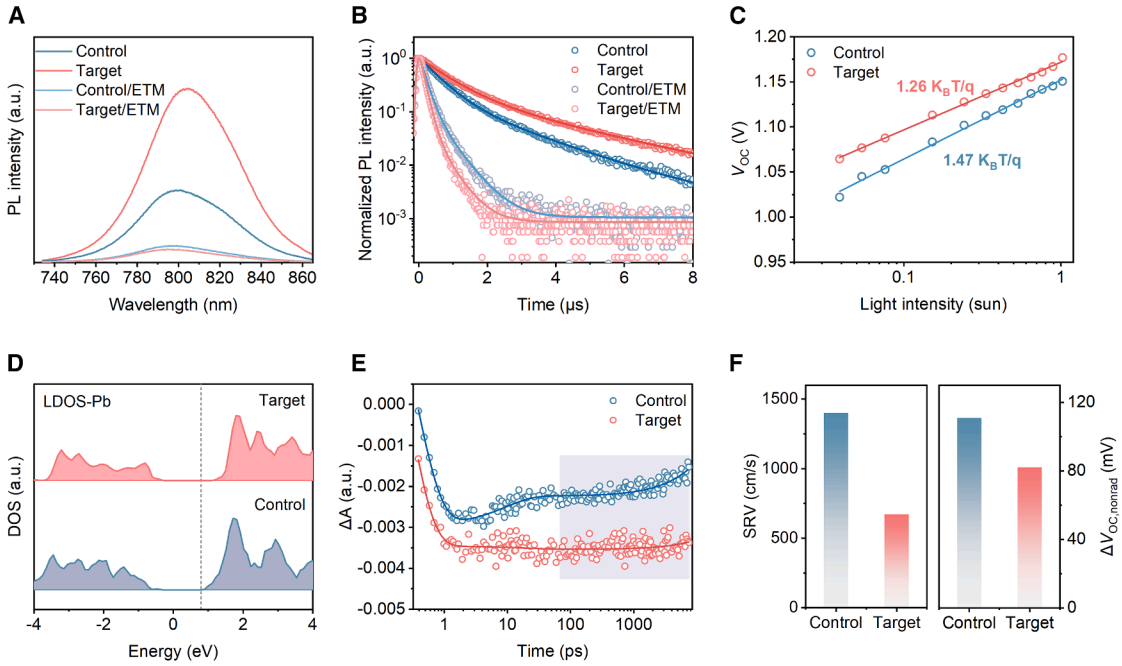

Figure 3. Reduced recombination losses after PO-T2T treatment

(A and B) SSPL and TRPL lifetimes of control and treated perovskite films with different stacks.

(C) Dependence of V_{OC} on light intensity for the control and treated PSCs. The slopes of the control and treated devices are 1.47 K_BT/q and 1.26 K_BT/q, respectively, indicating that the defect-assisted recombination is largely suppressed.

(D) Calculated LDOSs projected onto the surface Pb atoms of the control and PO-T2T-treated perovskites. With the PO-T2T molecule introduced, the surface Pb defect states are effectively passivated. This specific surface defect model provides direct evidence of the passivation mechanism enabled by our molecular coordination strategy.

(E) TA kinetics as a function of delay time for control and treated perovskite films following excitation at 400 nm (1 kHz, 100 fs, around 0.048 μJ cm^{-2}). The extended decay time of the treated film suggests that PO-T2T can significantly inhibit defect-assisted recombination.

(F) Calculated SRVs and nonradiative V_{OC} loss of control and treated perovskite films. The robust and stable BIEF successfully strengthens charge carrier separation and reduces defect accumulation.

recombination-induced V_{OC} loss ($\Delta V_{OC,\ nonrad}$) declines from 111 (control) to 82 (target) mV, attributed to the suppressed nonradiative recombination at the perovskite/ETL interface.[45] Collectively, these measurements consistently demonstrate that PO-T2T effectively passivates defects through molecular coordination, leading to a lower trap density and improved carrier dynamics, which successfully mitigate energy losses at the interface.

PV performance

To demonstrate the effect of PO-T2T on PV performance, we fabricated the p-i-n planar heterojunction PSCs with ITO/(4-(7H-dibenzo[c,g]carbazol-7-yl)butyl)phosphonic acid (4PADCB)/perovskite/lithium fluoride (LiF)/C_{60}/bathocuproine (BCP)/Ag architecture. The cross-sectional SEM image of the device is depicted in Figure 4A. Typical *J-V* scan curves of the devices without and with treatments recorded at simulated AM 1.5 G illumination conditions are shown in Figure 4B, and the corresponding PV parameters are summarized in Table S3. The best-performing target device achieves a PCE of 27.01% under reverse scan (V_{OC} = 1.179 V, J_{SC} = 26.26 mA cm^{-2}, and FF (fill factor) = 87.25%), which is higher than that of the control device (25.20%). This significant enhancement in device efficiency is attributed to a synergistic effect triggered by the molecular coordination. On the one hand, the formation of interfacial dipoles stabilizes the BIEF, enabling efficient charge extraction. On the other hand, the effective defect passivation reduces nonradiative recombination losses. Consequently, the simultaneous optimization drives the observed improvements in V_{OC} and FF, while maintaining high J_{SC}. In addition, the treated PSC exhibits a stabilized PCE of 26.45% under the maximum power point tracking (MPPT) for 500 s. The statistics of PV parameters in Figure S14 illustrate excellent device performance and batch-to-batch reproducibility. Moreover, we fabricated a large-area device (1.0 cm^2), which achieves a PCE of 24.44% with a V_{OC} of 1.190 V under reverse scan (Figure S15). We then evaluated the performance of the devices under multiple illumination intensities (0.1–2.1 sun), using a solar simulator with neutral density (ND) optical filters for attenuation and a condenser lens for light intensity enhancement. The observed non-monotonic dependence of efficiency on light intensity arises from the competition between trap-assisted nonradiative recombination (at low-intensity illumination) and illumination-induced electric field screening (at high-intensity illumination) within the device. Remarkably, the PO-T2T-incorporated device displays exceptional photostability, with a minimal efficiency decline of 5.8% relative to its

Please cite this article in press as: Chen et al., Molecular coordination stabilizes built-in electric fields for efficient perovskite solar cells, Joule (2026), https://doi.org/10.1016/j.joule.2026.102484

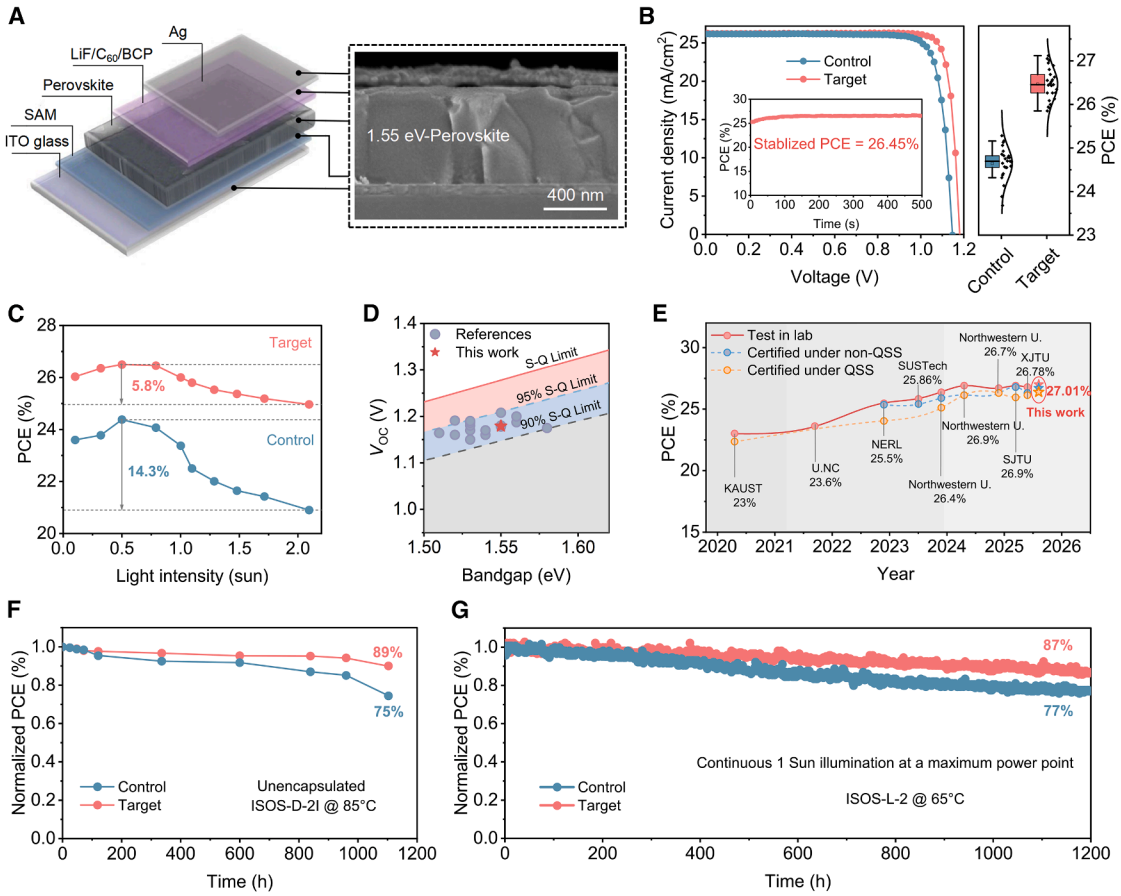

Figure 4. PV performance of PSCs

(A) Device structure and cross-sectional SEM image of the device.

(B) *J-V* curves and performance distributions of the control and PO-T2T-treated devices. The inset shows the stabilized PCE at the MPP for 500 s of the treated device.

(C) Evolution of the PV parameters for control and treated PSCs under multiple illumination intensities (0.1–2.1 sun). Light intensity is precisely attenuated using ND optical filters (Daheng Optics, T = 10%, 32%, 50%, and 79%) to simulate low-light conditions, while a condenser lens (Thorlabs) is employed to achieve high-light conditions. PCEs are averaged from three independent measurements, calculated as: $PCE = (V_{OC} \times J_{SC} \times FF / P_{in}) \times 100\%$. Compared with the control device, the minimal efficiency decline of the PO-T2T-treated device demonstrates that PO-T2T can effectively suppress the electric field screening effect under high-light conditions and thus stabilize the BIEF.

(D) Comparison of the V_{OC} with varied band gaps of high-performance PSCs reported so far.

(E) Efficiency evolution of state-of-the-art inverted PSCs reported in recent years.

(F) Thermal stability of unencapsulated control and treated devices aged at 85°C in a nitrogen atmosphere.

(G) Operational stability of encapsulated devices under continuous 1-sun illumination at 65°C in ambient air.

peak PCE under high-intensity illumination, in stark contrast to the control PSC, which shows a 14.3% efficiency reduction under identical conditions (Figure 4C). This significant difference provides direct experimental evidence that the PO-T2T treatment effectively suppresses electric field screening effects under illumination. More importantly, the outstanding light stability of PO-T2T-treated BIEF under high-intensity illumination makes it pivotal for designing efficient and stable PVs under concentrated sunlight.

We also performed FF loss analysis, as shown in Figure S16, which demonstrates a significant suppression of nonradiative loss and transport loss in the treated devices. Thus, in combination with the results of the V_{OC} loss analysis, we infer that the improved device performance can be ascribed to the improved stability of BIEF, which reduces the nonradiative recombination loss at the top perovskite surface. As shown in Figure 4D, the V_{OC} of our 1.55-eV devices reaches 90% of the theoretical limit, which is comparable to that of state-of-the-art inverted PSCs (Figure S17; Table S4). Furthermore, external quantum efficiency (EQE) spectra were collected for both devices and are plotted in Figure S18. The integrated current values are in accordance with the J_{SC} values extracted from the *J-V* curves. One of our best devices was sent to an accredited PV calibration center (National PV Industry Measurement and Testing Center), achieving a certified PCE of 26.71%, with V_{OC} of 1.174 V, J_{SC} of 26.25 mA cm^{-2}, FF of 86.69%, and a certified stabilized PCE of 26.38% (Figures S19–S21). Our developed molecular coordination strategy is equally effective for other perovskite compositions, such

Please cite this article in press as: Chen et al., Molecular coordination stabilizes built-in electric fields for efficient perovskite solar cells, Joule (2026), https://doi.org/10.1016/j.joule.2026.102484

as 1.58-eV and 1.64-eV wide-band-gap (WBG) PSCs. Notably, the PO-T2T-treated device exhibits an increased PCE from 23.30% to 25.30% for the 1.58-eV PSCs (Figure S22). Moreover, the PCE is improved by 8.9% when PO-T2T is applied to 1.64-eV WBG PSCs (Figure S23).

Next, we sought to investigate the impact of the PO-T2T on the stability of both films and devices. We exposed the unencapsulated films to ambient air and conducted XRD measurements to track their degradation. After 400 h, the control film shows a pronounced PbI_2 peak at 12.8°, whereas the PbI_2 content in the modified film remains negligible, indicating enhanced stability and suppressed phase transition, which aligns with the coordination effect of PO-T2T (Figure S24). We further monitored the thermal stability of the PSCs at 85°C following the ISOS-D-2I protocol. The target device degrades to 89% of its initial PCE after 1,100 h, whereas the control device exhibits ~25% PCE loss (Figures 4F and S25). Moreover, the stabilized BIEF by the molecular coordination strategy is also conducive to the operational stability of PSCs since it promotes interfacial carrier extraction. We then tested the operating stability of the encapsulated devices under MPPT at 65°C (ISOS-L-2 protocol). The PO-T2T-based PSC maintains 87% of its initial PCE after continuously operating for 1,200 h, surpassing the retention of 77% for the control device (Figure 4G).

DISCUSSION

We implemented this study with the understanding that the BIEF is easily screened by photoinjected carriers, leading to insufficient charge extraction and severe nonradiative recombination at the perovskite/C_{60} interface. This issue can be addressed by treating perovskite surface with PO-T2T to establish a BIEF through molecular coordination. The interactions between gradient-distributed PO-T2T and undercoordinated Pb^{2+} facilitate the redistribution of electrons, establishing a stable BIEF against the illumination screening. Our work shows that the reduction of recombination caused by stable BIEF leads to highly efficient and stable inverted PSCs. The findings of this research further underscore the significance of developing stable BIEF in advancing high-performance heterojunction solar cells and concentrator PVs.

METHODS

Materials

All the materials and reagents were used as received without any purification. Formamidinium iodide (FAI, 99.99%), methylammonium chloride (MACl, 99.99%), methylammonium bromide (MABr, 99.99%), and methylammonium iodide (MAI, 99.99%) were purchased from GreatCell Solar Materials. PbI_2 (99.99%) and lead (II) bromide ($PbBr_2$, 98%) were purchased from Tokyo Chemical Industry (TCI). Cesium iodide (CsI, 99.999%) was purchased from Sigma-Aldrich. 4PADCB (99%) was purchased from Suzhou LiWei Tech. PO-T2T (99.5%) and piperazinium iodide (PI, 99.5%) were purchased from Xi'an Yuri Solar. C_{60} (99.9%), BCP (99.5%), and LiF (99.99%) were purchased from Lumtec. N, N-dimethylformamide (DMF, anhydrous, 99.8%), dimethyl sulfoxide (DMSO, anhydrous, 99.9%), chlorobenzene (CB, anhydrous, 99.8%), isopropanol (IPA, anhydrous, 99.5%), and ethanol (anhydrous, 99.5%) were supplied by Sigma-Aldrich.

Perovskite precursor solutions

1.55 eV-$Cs_{0.05}FA_{0.85}MA_{0.1}PbI_3$: 1.66 M perovskite precursor solution composed of FAI, CsI, PbI_2 (10% of excess), and MAI was dissolved in 0.9 mL mixed solvent (DMF/DMSO = 4/1). Additionally, 10% MACl was added to the precursor. The solution was stirred for at least 2 h and subsequently filtered through a 0.22-μm polytetrafluoroethylene (PTFE) filter before use.

1.58 eV-$Cs_{0.05}(FA_{0.95}MA_{0.05})_{0.95}Pb(I_{0.95}Br_{0.05})_3$: 1.5 M perovskite precursor solution was prepared by dissolving 19.5 mg CsI, 7.97 mg MABr, 28.2 mg $PbBr_2$, 15.2 mg MACl, 232.5 mg FAI, and 718.3 mg PbI_2 in 1 mL mixed solvent (DMF/DMSO = 4/1). The solution was stirred for at least 2 h and subsequently filtered through a 0.22-μm PTFE filter before use.

1.64 eV-$Cs_{0.05}(FA_{0.83}MA_{0.17})_{0.95}Pb(I_{0.83}Br_{0.17})_3$: 18.7 mg CsI, 24.8 mg MABr, 81.6 mg $PbBr_2$, 191.1 mg FAI, and 563.5 mg PbI_2 were dissolved in 1 mL mixed solvent (DMF/DMSO = 4/1) to form 1.4 M stoichiometric solution. The solution was stirred for at least 2 h and then filtered through a 0.22-μm PTFE filter before use.

Device fabrication

The ITO glass substrates were ultrasonically cleaned with detergent solution, deionized water, acetone, and ethanol each for 10–15 min. The substrates were then treated with UV ozone for 15 min and transferred into an N_2 glove box. The HTL was fabricated by spin-coating 4PADCB (0.5 mg/mL in ethanol) on ITO glass at 3,000 rpm for 30 s, followed by annealing at 100°C for 10 min. The Al_2O_3 nanoparticle dispersion was spin-coated at 5,000 rpm for 30 s and annealed at 100°C for 10 min to enhance the wettability of the buried interface. After that, the perovskite solution was spin-coated at 4,000 rpm for 40 s (acceleration rate 800 rpm/s). CB (150 μL) was dropped onto the substrate during the 30 s of the step. For the treated samples, 0.15 mg/mL PO-T2T was dissolved in the CB solvent. The wet films were then annealed at 100°C for 30 min. A 0.3-mg/mL PI solution (in IPA) was spin-coated on the perovskite film surface at 5,000 rpm for 30 s, followed by annealing at 100°C for 5 min. Subsequently, LiF (1 nm), C_{60} (25 nm), and BCP (5 nm) were thermally evaporated on the perovskite films in high vacuum below 5×10^{-4} Pa. Finally, 110-nm Ag electrode was thermally evaporated at a rate of 1.5 Å s^{-1}.

Solar cells characterization

The *J-V* characteristics of the PSCs were measured using a Keithley 2400 source meter under simulated AM 1.5 G irradiation from an Xe lamp (Newport), and the light intensity was calibrated with a reference solar cell provided by NREL. The *J-V* curves were performed in a N_2 atmosphere by reverse scan (from 1.25 to −0.1 V) and forward scan (from −0.1 to 1.25 V). The active area of the aperture shade mask was certified by an accredited PV calibration center as 0.0517 cm^2. The EQE spectra were performed in ambient air, using a QE-R system (EnliTech).

Certification of PSCs

The PSCs were sent to the National PV Industry Measurement and Testing Center in Fujian, China, for independent certification. The PSCs were stored in a nitrogen-filled environment and kept in a dark container to prevent ambient light exposure. A mask with an aperture area of 0.0517 cm^2 was used during measurement.

Stability testing

For the ISOS-L-2 operating stability tests, the Bi/Cu electrodes (20/150 nm) used in the devices for stability testing were deposited via thermal evaporation at controlled rates of 0.1 Å s^{-1} for Bi and 0.1–0.5 Å s^{-1} for Cu. The operational stability of the encapsulated devices was evaluated using a commercial multichannel stability testing system (Wuhan 91PVKSolar), operating in MPPT mode at a temperature of 65°C. The encapsulation of the devices was performed following the methodology described in a previous report.[4,46] For ISOS-D-2I thermal stability tests, the unencapsulated devices were heated at 85°C in nitrogen.

Other characterization

The top-view SEM images were measured by Zeiss mini500 field-emission SEM. XRD was obtained by a Rigaku SmartLab diffractometer (Cu Kα radiation, λ = 1.5406 Å) at 40 kV and 200 mA. AFM and KPFM were conducted using Bruker equipment. The CPD was calculated by the following formula: $CPD = \frac{W_{tip} - W_{sample}}{-e}$. The UV-vis absorption spectra were taken with a Shimadzu UV-1750 spectrophotometer. XPS and UPS data were collected by using Thermo Fisher Scientific ESCALAB Xi^+. The steady-state photoluminescence (SSPL) spectra were performed using a fluorescence spectrophotometer (SP-2300, Princeton Instruments) with an excitation wavelength of 600 nm. TRPL spectra were conducted on a streak camera system (C10910, HAMAMATSU). For both measurements, the films were deposited on quartz substrates. fs-TA spectra were measured with a Helios Ultrafast Systems LLC TA spectrometer. The pump pulse was generated with a collinear optical parametric amplifier (OPerA Solo, Coherent), which was pumped by 800 nm fundamental pulses (150 fs, 1 kHz). The laser pulses at 400 nm were generated by using BBO (β-BaB_2O_4) crystals. TOF-SIMS was measured with the TOF-SIMS 5-100 instrument. Mott-Schottky plots measurements were carried out using an electrochemical workstation in impedance-potential mode. The space charge limited current (SCLC) measurements were conducted with a structure of ITO/SAM/perovskite/spiro-OMeTAD/Ag in the dark. The FTIR spectra of powders and perovskite films were obtained using Bruker (TENSOR II) equipment. External electroluminescence quantum efficiency (EQE_{EL}) measurement was recorded with a spectrometer (Ocean Optics USB2000+) with a step of 0.05 V.

Theoretical calculation

DFT calculations are performed using the Vienna Ab Initio Simulation Packages (VASP) with the generalized gradient approximation (GGA) proposed by Perdew-Burke-Ernzerhof (PBE).[47] The structure relaxations are carried out with 450 eV plane-wave cutoff, and the van der Waals force correction is considered with the DFT-D3 method of Grimme.[48] The Brillouin zone integration was sampled following a gamma-centered Monkhorst-Pack scheme,[49] using 1 × 1 × 1 k-point grids for ionic optimization and 3 × 3 × 3 k-point grids for the density of state. The self-consistent total-energy difference and the convergence criterion for forces on atoms are set to 10^{-4} eV and 0.01 eV $Å^{-1}$, respectively. We used a vacuum over 15 Å to adequately separate images along the surface normal direction. Electrostatic surface potential (ESP) and electric dipole moment (EDM) analyses were performed. Geometric optimization was carried out by utilizing the Gaussian 09 package using the PBE0 density functional along with the B3LYP/6-31G(d) basis set.

RESOURCE AVAILABILITY

Lead contact

Further information and requests for resources should be directed to and will be fulfilled by the lead contact, Guichuan Xing (gcxing@um.edu.mo).

Materials availability

This study did not generate new, unique materials.

Data and code availability

This study did not generate any datasets or codes.

ACKNOWLEDGMENTS

This work was supported by the Science and Technology Development Fund, Macao SAR (file no. 0060/2023/RIA1, 0046/2025/RIB1, 0148/2024/RIA2, 0042/2025/RIA1, 0136/2022/A3, 0122/2024/AMJ, and 0002/2024/TFP); the UM's Research Fund (file no. MYRG-GRG2024-00156-IAPME, MYRG-CRG2025-0024-IAPME, and MYRG-GRG2025-00259-IAPME); the Guangdong Provincial Basic and Applied Basic Research Foundation (grant no. 2025B0303000002); the Natural Science Foundation of China (62175268, 62288102, 22405010, 62275162, 1204441, 62205384, 22579136, and 62304111); the Shenzhen Science and Technology Program (no. JCYJ20241202124510014); the National Key Research and Development Program of China (2024YFE0201800); the Shaanxi Fundamental Science Research Project for Mathematics and Physics (22JSY015 and 23JSY005); the Young Talent Fund of Xi'an Association for Science and Technology (959202313020); the Shaanxi Province Science and Technology Activities for Overseas Students selected funding project (2023015); the Youth Project in Natural Science and Engineering Technology (2023SYJ15 and 2023SYJ25); the Guangdong Provincial Key Laboratory of Semiconductor optoelectronic Materials and Intelligent Photonic Systems (no. 2023B1212010003); and the China Postdoctoral Science Foundation (no. 2024M761492).

AUTHOR CONTRIBUTIONS

Conceptualization, Y.C., D.Y., and G.X.; methodology, Y.C., D.Y., X.Q., H.G., J.G., Y. Lin, B.W., J.X., T.S., S.L., and T.-W.L.; investigation, Y.C., D.Y., and G.X.; visualization, Y.C., D.Y., X.Q., and H.G.; stability testing, Y. Lin and C.L.; DFT calculations, J.X.; PL testing, B.W.; funding acquisition, B.W., J.X., C.L., Y. Li, and G.X.; project administration, J.G., S.C., C.L., Y. Li, and G.X.; supervision, Y. Li and G.X.; writing – original draft, Y.C., D.Y., and G.X.; writing – review and editing, D.Y., H.G., J.G., J.X., C.L., Y. Li, and G.X. All authors discussed the results and commented on the manuscript.

DECLARATION OF INTERESTS

The authors declare no competing interests.

SUPPLEMENTAL INFORMATION

Supplemental information can be found online at https://doi.org/10.1016/j.joule.2026.102484.

Received: November 4, 2025
Revised: February 12, 2026
Accepted: April 20, 2026

REFERENCES

1. Yu, S.Q., Xiong, Z., Zhou, H.T., Zhang, Q., Wang, Z.H., Ma, F., Qu, Z.H., Zhao, Y., Chu, X.B., Zhang, X.W., et al. (2023). Homogenized NiO_X nanoparticles for improved hole transport in inverted perovskite solar cells. Science *382*, 1399–1404. https://doi.org/10.1126/science.adj8858.
2. Chen, H., Liu, C., Xu, J., Maxwell, A., Zhou, W., Yang, Y., Zhou, Q., Bati, A.S.R., Wan, H., Wang, Z., et al. (2024). Improved charge extraction in inverted perovskite solar cells with dual-site-binding ligands. Science *384*, 189–193. https://doi.org/10.1126/science.adm9474.
3. Kojima, A., Teshima, K., Shirai, Y., and Miyasaka, T. (2009). Organometal halide perovskites as visible-light sensitizers for photovoltaic cells. J. Am. Chem. Soc. *131*, 6050–6051. https://doi.org/10.1021/ja809598r.
4. Lin, Y., Lin, Z., Lv, S., Shui, Y., Zhu, W., Zhang, Z., Yang, W., Zhao, J., Gu, H., Xia, J., et al. (2025). A Nd@C_{82}–polymer interface for efficient and stable perovskite solar cells. Nature *642*, 78–84. https://doi.org/10.1038/s41586-025-08961-9.
5. Al-Ashouri, A., Köhnen, E., Li, B., Magomedov, A., Hempel, H., Caprioglio, P., Márquez, J.A., Morales Vilches, A.B., Kasparavicius, E., Smith, J.A., et al. (2020). Monolithic perovskite/silicon tandem solar cell with >29% efficiency by enhanced hole extraction. Science *370*, 1300–1309. https://doi.org/10.1126/science.abd4016.
6. Yang, G., Ni, Z., Yu, Z.J., Larson, B.W., Yu, Z., Chen, B., Alasfour, A., Xiao, X., Luther, J.M., Holman, Z.C., et al. (2022). Defect engineering in wide-bandgap perovskites for efficient perovskite–silicon tandem solar cells. Nat. Photonics *16*, 588–594. https://doi.org/10.1038/s41566-022-01033-8.
7. Zhu, H.W., Teale, S., Lintangpradipto, M.N., Mahesh, S., Chen, B., McGehee, M.D., Sargent, E.H., and Bakr, O.M. (2023). Long-term operating stability in perovskite photovoltaics. Nat. Rev. Mater. *8*, 569–586. https://doi.org/10.1038/s41578-023-00582-w.
8. Liu, S.W., Li, J.B., Xiao, W.S., Chen, R., Sun, Z.X., Zhang, Y., Lei, X., Hu, S.F., Kober-Czerny, M., Wang, J.N., et al. (2024). Buried interface molecular hybrid for inverted perovskite solar cells. Nature *632*, 536–542. https://doi.org/10.1038/s41586-024-07723-3.
9. Liu, S.W., Biju, V.P., Qi, Y.B., Chen, W., and Liu, Z.H. (2023). Recent progress in the development of high-efficiency inverted perovskite solar cells. NPG Asia Mater. *15*, 27. https://doi.org/10.1038/s41427-023-00474-z.
10. Xiao, Y., Yang, X.Y., Zhu, R., and Snaith, H.J. (2024). Unlocking interfaces in photovoltaics. Science *384*, 846–848. https://doi.org/10.1126/science.adh8086.
11. Zhang, S., Ye, F., Wang, X., Chen, R., Zhang, H., Zhan, L., Jiang, X., Li, Y., Ji, X., Liu, S., et al. (2023). Minimizing buried interfacial defects for efficient inverted perovskite solar cells. Science *380*, 404–409. https://doi.org/10.1126/science.adg3755.
12. Li, Z., Sun, X.L., Zheng, X.P., Li, B., Gao, D.P., Zhang, S.F., Wu, X., Li, S., Gong, J.Q., Luther, J.M., et al. (2023). Stabilized hole-selective layer for high-performance inverted p-i-n perovskite solar cells. Science *382*, 284–289. https://doi.org/10.1126/science.ade9637.
13. Zhang, X., Wu, S., Zhang, H., Jen, A.K.Y., Zhan, Y., and Chu, J. (2024). Advances in inverted perovskite solar cells. Nat. Photonics *18*, 1243–1253. https://doi.org/10.1038/s41566-024-01541-9.
14. Zhao, T.Q., Shi, W., Xi, J.Y., Wang, D., and Shuai, Z.G. (2016). Intrinsic and extrinsic charge transport in $CH_3NH_3PbI_3$ perovskites predicted from first-principles. Sci. Rep. *7*, 19968. https://doi.org/10.1038/srep19968.
15. Wu, J., Cha, H., Du, T., Dong, Y., Xu, W., Lin, C.-T., and Durrant, J.R. (2022). A comparison of charge carrier dynamics in organic and perovskite solar cells. Adv. Mater. *34*, e2101833. https://doi.org/10.1002/adma.202101833.
16. Johnston, M.B., and Herz, L.M. (2016). Hybrid perovskites for photovoltaics: charge-carrier recombination, diffusion, and radiative efficiencies. Acc. Chem. Res. *49*, 146–154. https://doi.org/10.1021/acs.accounts.5b00411.
17. Milot, R.L., Eperon, G.E., Snaith, H.J., Johnston, M.B., and Herz, L.M. (2015). Temperature-dependent charge-carrier dynamics in $CH_3NH_3PbI_3$ perovskite thin films. Adv. Funct. Mater. *25*, 6218–6227. https://doi.org/10.1002/adfm.201502340.
18. Hasegawa, T., and Kojima, O. (2024). Effects of electric field screening induced by photogenerated carriers on terahertz wave measurement in a GaAs epitaxial structure. Appl. Phys. Express *17*, 051006. https://doi.org/10.35848/1882-0786/ad3ee1.
19. Murakami, H., Fujiwara, S., Kawayama, I., and Tonouchi, M. (2016). Study of photoexcited-carrier dynamics in GaAs photoconductive switches using dynamic terahertz emission microscopy. Photonics Res. *4*, A9. https://doi.org/10.1364/PRJ.4.0000A9.
20. Zhu, H.W., Shao, B.Y., Shen, Z.J., You, S., Yin, J., Wehbe, N., Wang, L.J., Song, X., Abulikemu, M., Basaheeh, A., et al. (2025). In situ energetics modulation enables high-efficiency and stable inverted perovskite solar cells. Nat. Photonics *19*, 28–35. https://doi.org/10.1038/s41566-024-01542-8.
21. Wang, K.L., Zhou, Y.H., Lou, Y.H., and Wang, Z.K. (2021). Perovskite indoor photovoltaics: opportunity and challenges. Chem. Sci. *12*, 11936–11954. https://doi.org/10.1039/D1SC03251H.
22. Guo, Z.L., Jena, A.K., and Miyasaka, T. (2023). Halide perovskites for indoor photovoltaics: the next possibility. ACS Energy Lett. *8*, 90–95. https://doi.org/10.1021/acsenergylett.2c02268.
23. Pei, F.T., Chen, Y.H., Wang, Q.Q., Li, L., Ma, Y., Liu, H.F., Duan, Y., Song, T.L., Xie, H.P., Liu, G.L., et al. (2024). A binary 2D perovskite passivation for efficient and stable perovskite/silicon tandem solar cells. Nat. Commun. *15*, 7024. https://doi.org/10.1038/s41467-024-51345-2.
24. Gu, H., Zhu, A.N., Xia, J.M., Li, W., Zheng, J.H., Yang, T., Li, S.W., Zhang, N., Mei, S.L., Cai, Y.Q., et al. (2024). Nanoscale phase management of the 2D/3D heterostructure toward efficient perovskite solar cells. Sci. Bull. *69*, 2853–2861. https://doi.org/10.1016/j.scib.2024.07.026.
25. Li, S.W., Gu, H., Zhu, A.N., Guo, J., Xi, C.P., Qiu, X.S., Chen, Y., Pan, H., Chen, J.Z., Xing, G.C., et al. (2025). Anion-cation synergistic regulation of low-dimensional perovskite passivation layer for perovskite solar cells. Adv. Mater. *37*, e2500988. https://doi.org/10.1002/adma.202500988.
26. Chen, W., Liu, S., Li, Q., Cheng, Q., He, B., Hu, Z., Shen, Y., Chen, H., Xu, G., Ou, X., et al. (2022). High-polarizability organic ferroelectric materials doping for enhancing the built-in electric field of perovskite solar cells realizing efficiency over 24%. Adv. Mater. *34*, e2110482. https://doi.org/10.1002/adma.202110482.
27. Wang, W.T., Chen, P., Chiang, C.H., Guo, T.F., Wu, C.G., and Feng, S.P. (2020). Synergistic reinforcement of built-In electric fields for highly efficient and stable perovskite photovoltaics. Adv. Funct. Mater. *30*, 1909755. https://doi.org/10.1002/adfm.201909755.
28. Chen, J., Yang, Y., Dong, H., Li, J., Zhu, X., Xu, J., Pan, F., Yuan, F., Dai, J., Jiao, B., et al. (2022). Highly efficient and stable perovskite solar cells enabled by low-dimensional perovskitoids. Sci. Adv. *8*, eabk2722. https://doi.org/10.1126/sciadv.abk2722.
29. Mazumdar, S., Zhao, Y., and Zhang, X. (2021). Stability of perovskite solar cells: degradation mechanisms and remedies. Front. Electron. *2*, 712785. https://doi.org/10.3389/felec.2021.712785.
30. Na Quan, L., Ma, D., Zhao, Y., Voznyy, O., Yuan, H., Bladt, E., Pan, J., García de Arquer, F.P., Sabatini, R., Piontkowski, Z., et al. (2020). Edge stabilization in reduced-dimensional perovskites. Nat. Commun. *11*, 170. https://doi.org/10.1038/s41467-019-13944-2.
31. Chen, S.S., Xiao, X., Chen, B., Kelly, L.L., Zhao, J.J., Lin, Y.Z., Toney, M.F., and Huang, J.S. (2021). Crystallization in one-step solution deposition of perovskite films: Upward or downward? Sci. Adv. *7*, eabb2412. https://doi.org/10.1126/sciadv.abb2412.

32. Zhang, Z.L., Feng, Y.S., Ding, J.K., Ma, Q.X., Zhang, H., Zhang, J.J., Li, M.J., Geng, T.R., Gao, W.H., Wang, Y., et al. (2025). Rationally designed universal passivator for high-performance single-junction and tandem perovskite solar cells. Nat. Commun. *16*, 753. https://doi.org/10.1038/s41467-025-56068-6.

33. Sutanto, A.A., Caprioglio, P., Drigo, N., Hofstetter, Y.J., Garcia-Benito, I., Queloz, V.I.E., Neher, D., Nazeeruddin, M.K., Stolterfoht, M., Vaynzof, Y., et al. (2021). 2D/3D perovskite engineering eliminates interfacial recombination losses in hybrid perovskite solar cells. Chem *7*, 1903–1916. https://doi.org/10.1016/j.chempr.2021.04.002.

34. Zheng, Y.T., Li, Y.R., Zhuang, R.S., Wu, X.Y., Tian, C.C., Sun, A.X., Chen, C., Guo, Y.S., Hua, Y., Meng, K., et al. (2024). Towards 26% efficiency in inverted perovskite solar cells via interfacial flipped band bending and suppressed deep-level traps. Energy Environ. Sci. *17*, 1153–1162. https://doi.org/10.1039/D3EE03435F.

35. Li, H., Chang, B.H., Wang, L., Wang, Z.X., Pan, L., Wu, Y.T., Liu, Z., and Yin, L.W. (2022). Surface reconstruction for tin-based perovskite solar cells. ACS Energy Lett. *7*, 3889–3899. https://doi.org/10.1021/acsenergylett.2c01624.

36. Wu, T.H., Liu, X., Luo, X.H., Segawa, H., Tong, G.Q., Zhang, Y.Q., Ono, L.K., Qi, Y.B., and Han, L.Y. (2022). Heterogeneous $FASnI_3$ absorber with enhanced electric field for high-performance lead-free perovskite solar cells. Nano-Micro Lett. *14*, 99. https://doi.org/10.1007/s40820-022-00842-4.

37. Li, X.D., Zhang, W.X., Guo, X.M., Lu, C.Y., Wei, J.Y., and Fang, J.F. (2022). Constructing heterojunctions by surface sulfidation for efficient inverted perovskite solar cells. Science *375*, 434–437. https://doi.org/10.1126/science.abl5676.

38. Zhang, W.Y., He, L., Meng, Y., Kanda, H., Tang, D.Y., Ding, B., Ding, Y., Nazeeruddin, M.K., and Li, X. (2022). Dual-site synergistic passivation for highly efficient and stable perovskite solar cells. Adv. Energy Mater. *12*, 2202189. https://doi.org/10.1002/aenm.202202189.

39. Xiong, W.T., Tang, W.D., Zhang, G., Yang, Y.C., Fan, Y.N., Zhou, K., Zou, C., Zhao, B.D., and Di, D.W. (2024). Controllable p- and n-type behaviours in emissive perovskite semiconductors. Nature *633*, 344–350. https://doi.org/10.1038/s41586-024-07792-4.

40. Wang, R., Xue, J.J., Wang, K.L., Wang, Z.K., Luo, Y.Q., Fenning, D., Xu, G.W., Nuryyeva, S., Huang, T.Y., Zhao, Y.P., et al. (2019). Constructive molecular configurations for surface-defect passivation of perovskite photovoltaics. Science *366*, 1509–1513. https://doi.org/10.1126/science.aay9698.

41. Lu, D.Z., Wang, X.Y., Hu, Y.J., Yue, L.G., Shao, Z.H., Zhou, W.L., Chen, L., Wang, W., and Li, Y.Y. (2023). Expediting stepwise sulfur conversion via spontaneous built-in electric field and binary sulfiphilic effect of conductive NbB_2-MXene heterostructure in lithium-sulfur batteries. Adv. Funct. Mater. *33*, 2212689. https://doi.org/10.1002/adfm.202212689.

42. Yu, D.J., Cao, F., Liao, J.F., Wang, B.Z., Su, C.L., and Xing, G.C. (2022). Direct observation of photoinduced carrier blocking in mixed-dimensional 2D/3D perovskites and the origin. Nat. Commun. *13*, 6229. https://doi.org/10.1038/s41467-022-33752-5.

43. Huang, Y.L., Liu, T.H., Wang, B.Z., Li, J.L., Li, D.Y., Wang, G.L., Lian, Q., Amini, A., Chen, S., Cheng, C., et al. (2021). Antisolvent engineering to optimize grain crystallinity and hole-blocking capability of perovskite films for high-performance photovoltaics. Adv. Mater. *33*, e2102816. https://doi.org/10.1002/adma.202102816.

44. Wang, J., Fu, W., Jariwala, S., Sinha, I., Jen, A.K.Y., and Ginger, D.S. (2019). Reducing surface recombination velocities at the electrical contacts will improve perovskite photovoltaics. ACS Energy Lett. *4*, 222–227. https://doi.org/10.1021/acsenergylett.8b02058.

45. Li, Z., Li, B., Wu, X., Sheppard, S.A., Zhang, S.F., Gao, D.P., Long, N.J., and Zhu, Z.L. (2022). Organometallic-functionalized interfaces for highly efficient inverted perovskite solar cells. Science *376*, 416–420. https://doi.org/10.1126/science.abm8566.

46. Lin, R.X., Wang, Y.R., Lu, Q.W., Tang, B.B., Li, J.Y., Gao, H., Gao, Y., Li, H.J., Ding, C.Z., Wen, J., et al. (2023). All-perovskite tandem solar cells with 3D/3D bilayer perovskite heterojunction. Nature *620*, 994–1000. https://doi.org/10.1038/s41586-023-06278-z.

47. Perdew, J.P., Burke, K., and Ernzerhof, M. (1996). Generalized gradient approximation made simple. Phys. Rev. Lett. *77*, 3865–3868. https://doi.org/10.1103/PhysRevLett.77.3865.

48. Kresse, G., and Joubert, D. (1999). From ultrasoft pseudopotentials to the projector augmented-wave method. Phys. Rev., B *59*, 1758–1775. https://doi.org/10.1103/PhysRevB.59.1758.

49. Monkhorst, H.J., and Pack, J.D. (1976). Special points for Brillouin-zone integrations. Phys. Rev., B *13*, 5188–5192. https://doi.org/10.1103/PhysRevB.13.5188.